J. Biophotonics **8**, No. 1–2, 81–93 (2015) / **DOI** 10.1002/jbio.201300140

Journal of BIOPHOTONICS

FULL ARTICLE

Photoacoustic and photothermal cytometry using photoswitchable proteins and nanoparticles with ultrasharp resonances

Ekaterina I. Galanzha[1], *Dmitry A. Nedosekin*[1], *Mustafa Sarimollaoglu*[1], *Anamaria Ioana Orza*[2], *Alexandru S. Biris*[2], *Vladislav V. Verkhusha*[3], *and Vladimir P. Zharov*[*,1]

[1] Arkansas Nanomedicine Center, University of Arkansas for Medical Sciences, 4301 West Markham Street, Slot #543, Little Rock, Arkansas 72205, USA
[2] Center for Integrative Nanotechnology Sciences, University of Arkansas at Little Rock, Arkansas 72204, USA
[3] Department of Anatomy and Structural Biology, and Gruss-Lipper Biophotonics Center, Albert Einstein College of Medicine, Bronx, New York 10461, USA

Received 29 August 2013, revised 18 October 2013, accepted 18 October 2013
Published online 19 November 2013

Key words: photoswitchable fluorescent proteins, photothermal and photoacoustic spectroscopy, photothermal switching, plasmonic nanoparticles, ultrasharp spectral resonances, *in vivo* flow cytometry, circulating cells

Photoswitchable fluorescent proteins (PSFPs) with controllable spectral shifts in emission in response to light have led to breakthroughs in cell biology. Conventional photoswitching, however, is not applicable to weakly fluorescent proteins. As an alternative, photothermal (PT) and photoacoustic (PA) spectroscopy have demonstrated a tremendous potential for studying absorbing nonfluorescent proteins and nanoparticles. However, little progress has been made in the development of switchable PT and PA probes with controllable spectral shifts in absorption. Here, we introduce the concept of photothermally switchable nanoparticles (PTSNs). To prove the concept, we demonstrated fast, reversible magnetic–PT switching of conventional and gold-coated magnetic nanoparticle clusters in cancer cells *in vitro* and PT switching of nonlinear ultrasharp plasmonic resonances in gold nanorods molecularly targeted to circulating cells *in vivo*. We showed that genetically encoded PSFPs with relatively slow switching can serve as triple-modal fluorescent, PT, and PA probes under static conditions, while PTSNs with ultrafast switching may provide higher PA sensitivity in the near-infrared window of tissue transparency under dynamic flow conditions. Application of nonlinear phenomena for super-resolution spectral PT and PA cytometry, microscopy, and spectral burning beyond the diffraction and spectral limits are also proposed.

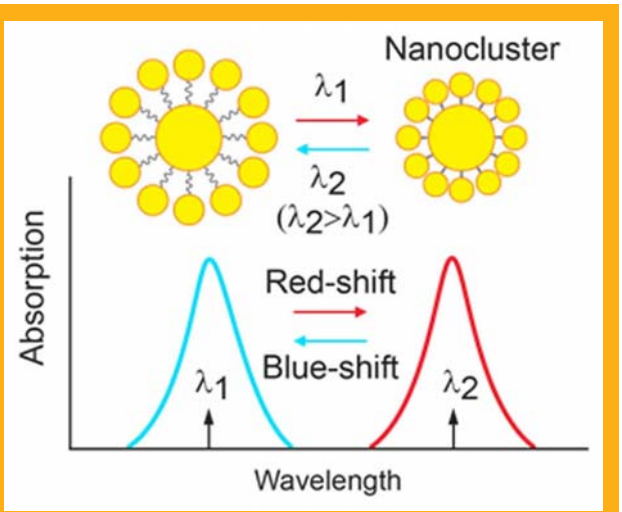

Principle of photothermally switchable PT and PA contrast agents. The example of switching of collective plasmonic resonances by controllable spatial relocation of nanoparticles in clusters.

* Corresponding author: e-mail: zharovvladimirp@uams.edu, Phone: (501) 603-1213

Journal of BIOPHOTONICS

1. Introduction

Laser-based optical imaging represents an unprecedented recent advance that has revolutionized cell biology and medicine [1, 2]. Among the different optical methods, fluorescence imaging using advanced labels remains the most powerful biological tool. The development of genetically encoded photoswitchable (also termed photoconvertible) fluorescent proteins (PSFPs) [3–17] that can control spectral shifts in emission in response to light of a specific wavelength and dose has led to breakthroughs in cell biology. These include tracking of protein dynamics in living cells, tracing of the shape of neurons, metabolic study of tumor cells, cell trafficking, and high-throughput biological screening with the use of both conventional optical imaging and super-resolution microscopy with stochastic optical reconstruction (STORM) and photoactivated localization (PALM) schematics [1].

Monomeric Dendra2, mEos2, and mKikGR are currently among the best available Kaede-like PSFPs, which are converted from green to red fluorescent form with exposure to violet light [14, 15]. Recently, a rational design was applied to conventional monomeric cyan fluorescent proteins, resulting in a green-to-red mClavGR2 PSFP [11]. On the basis of the EosFP and Dendra2 variants, several PSFPs with complex phenotypes exhibiting properties of both irreversible and reversible PSFPs have been developed. Similarly to Kaede-like PSFPs, irreversible photoswitching of IrisFP and NijiFP to green and red forms occurs simultaneously [6, 13]. Subsequent irradiation of the green forms of these PSFPs with a 488 nm or a low-intensity 405 nm laser reversibly switches their green chromophore off or on, respectively. Irradiation of the red forms with 532 nm light drives the red chromophores into the off state, whereas irradiation with 440 nm light switches them on. The recently developed monometric PSmOrange and PSmOrange2 are orange in their initial states and become far-red after irradiation with blue-green light [14, 15].

Despite significant progress in the development of PSFPs, their application in animal models *in vivo* is still burdened with challenges. Among these are the phototoxicity of violet light used to photoconvert Kaede-like PSFPs, its low penetration into tissue ($\leq$500 μm), and its photobleaching. In addition, the photoconversion time is too long (0.5–10 sec) for dynamic study, and PSFPs have still limited capability for excitation and emission in the near-infrared (NIR) optical window of relative transparency of mammalian tissues (700–900 nm).

As an alternative, photothermal (PT) and, especially, photoacoustic (PA) methods based on nonradiative relaxation of absorbed energy into heat and acoustic waves has demonstrated tremendous potential in biological and clinical applications for studies of nonfluorescent proteins, neuron receptors, mitochondrial morphology, cell-surface markers, gene reporters, and antigen – antibody reactions, as well as *in vivo* imaging of breast tumor cells and monitoring of oxygenation in large neck vessels in humans [18–46]. The molecular specificity of PT and PA methods is provided by small (5–30 nm), low-toxicity, tunable, functionalized NIR nanoparticles (NPs), including gold nanorods (GNRs), gold nanoshells (GNSs), golden carbon nanotubes (GNTs), and several others; some of these NPs have been approved for pilot studies in humans [18, 23–26]. Despite progress in the development of advanced metal NPs for use in biological labeling, photonics, optoelectronics, information storage, various imaging modalities, microscopy, cytometry [47–57], and particularly PA-PT nano-theranostics (nanotechnology-based integration of PA diagnosis and PT therapy) [27, 38, 44, 45], little progress has been made in the development of switchable NPs. This places many nanotechnology-based nonfluorescent imaging methods (e.g., absorption, PT, and PA) and nanotechnology at a great disadvantage as compared to fluorescence probes and imaging. Photothermally switchable NPs (PTSNs) described in this paper can help overcome this disadvantage by the use of ultrafast, PT-based shifting of the absorption spectra of PT and PA nanoprobes with linear and nonlinear dynamic, ultrasharp PT and PA plasmonic resonances and magnetic properties. Because so little progress has been made in exploring even conventional PSFPs as PT and PA contrast agents, we performed additional studies comparing the potential of PSFPs and PTSNs in PT and PA spectroscopy and cytometry.

2. Materials and methods

2.1 Concept of PT switching of nonfluorescent probes

The concept of PTSNs, especially plasmonic NPs, assumes that the absorption spectra of NPs can undergo ultrafast spectral shifts in response to short laser pulses of different wavelengths inducing linear and nonlinear PT-PA effects alone or in combination with photochemical, magnetic, and clustering phenomena.

2.1.1 PT switching of nanoclusters

This approach is based on exploring plasmonic reversible-cascade phenomena, with a focus on the

coupling of different plasmon modes of NPs with different shapes (e.g., spheres, rods, or shells), sizes, compositions (Au, Fe, Ag, or TiO_2), and spatial (1-, 2-, and 3-D) architectures (e.g., chain or multilayer). The location and intensity of plasmonic absorption resonances of individual gold NPs depend on their size and shape and surrounding dielectric and optical properties [30–33]. The spectral position of plasmonic resonances of closely located NPs depends additionally on the distances between the NPs [45]. We propose that one of the switching mechanisms can be based on controllable NP clustering and NP disaggregation accompanied by red or blue shifts in absorption, respectively (Figure 1A). In particular, irradiation of assemblages of NPs with a relatively low laser pulse energy can enhance their clustering by thermally modifying the NPs (e.g., melting or fusing them or partly exploding their surface, which leads to condensation of NP fragments on nearby NPs [30]) or by removing polymer layers or even ligands (e.g., antibodies) from them as the main barriers preventing their complete attachment to each other [29]. On the other hand, irradiation of self-assembled NP clusters at relatively high pulse energy levels can lead to NP-cluster disintegration by thermally expanding NPs and/or laser-induced nanobubbles around individual NPs, or to NP fragmentation

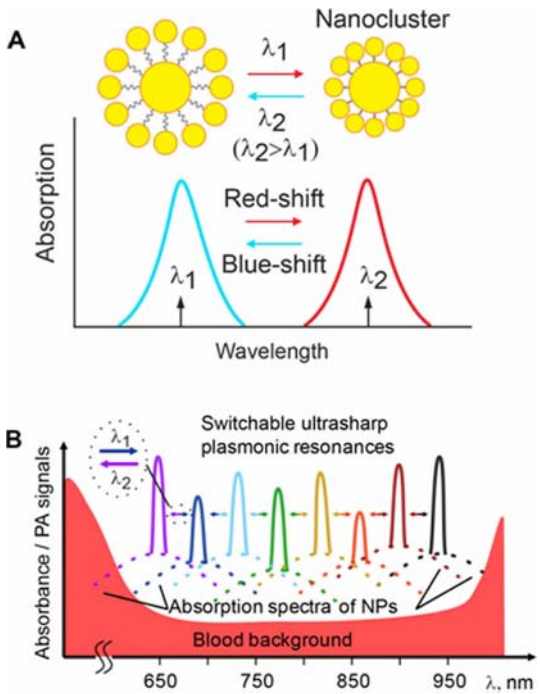

Figure 1 Principle of photothermally switchable PT and PA contrast agents. (**A**) Spectral switching of collective plasmonic resonances by laser manipulation of the spatial assembly of NP clusters. (**B**) Switching of multiple ultrasharp nonlinear resonances in a plasmonic NP cocktail.

[29, 30, 34, 39], which pushes NPs away from each other.

The individual gold NPs can also be connected by light-sensitive materials (e.g., protein, polymer) as adjustable "strings". Laser-induced temperature- or photochemical-dependent reversible changes in the distances between individual NPs in clusters are accompanied by blue and red shifts in collective plasmon resonances as interparticle distances increase and decrease, respectively. Another approach is to explore electrochemical switching of NP-polymer constructs by using the polymer's reduced and oxidized states [47] or by using photochromism phenomena in porous silica NPs loaded with TiO_2 and Ag (or Au) matrix, which absorbs in the visible range [52, 53]. Laser-induced photogeneration of electrons in TiO_2 will lead to formation of Ag–NP clusters with red-shifted absorption in the NIR range. A second laser pulse in the NIR range will disintegrate the Ag–NP clusters into individual Ag NPs or even to atoms, thus returning the color back to the visible range.

2.1.2 PT modification of NP size and shape

PTSNs can be based on laser-induced modification of the size and shape of gold NPs through melting and explosion. With increases in the laser pulse energy level, the temperatures of the NPs may quickly reach the thresholds of phase effects, including evaporation of the liquid surrounding heated NPs (250 to 350 °C for water), bulk melting of NPs (1,063 °C for gold), and NP evaporation (2,710 °C for gold) [28, 30, 39]. Melting of the surface of an NP, which creates a liquid surface layer, can occur at a lower temperature than that required for bulk melting (e.g., $\leq$300 °C) [31, 32]. Due to fast nonradiative relaxation [32], temperature-dependent changes of gold-NP shapes or sizes in response to laser pulses starting at the picosecond scale (5–10 psec) lead to blue- or red-spectral shifts in absorption, and hence to PT and PA spectra depending on NP type. For example, laser-induced heat changes the shape of GNRs from cylindrical to ellipsoidal at relatively low pulse energy levels close to their melting threshold, and to spherical at higher energy levels [33]. These modifications to GNRs are accompanied by blue-spectral shifts because maximum absorption for ellipsoidal and spherical NPs occurs at shorter wavelengths than those for intact GNRs with plasmonic resonances at longer wavelengths. Thus, absorption and PT and PA signals decrease at longer wavelengths and increase at shorter wavelengths relative to the center of plasmonic resonances in GNRs [31–33]. These NP modifications can occur during short (from picosecond to nanosecond) laser pulses and

even at the beginning of relatively longer laser pulses that can eventually lead to PT and PA blue-spectral shifts. Red and blue shifts occur in GNSs because of laser-induced decreases and increases, respectively, in the thickness of the gold shell around the silica core (e.g., by Au evaporation or condensation) or because of extensive melting and formation of gold nanospheres on the surface of GNSs [34].

2.1.3 Magnetic switching

Functionalized magnetic NPs (MNPs) can be used as multifunctional PT and PA contrast agents for molecular targeting of circulating tumor cells (CTCs) or bacteria *in vivo* directly in the bloodstream, and then captured with a magnet attached to the skin above vessels [35–38]. In particular, magnet-induced PT and PA signal amplification from individual cancer cells and bacteria can reach up to 10-fold [36]. One possible mechanism responsible for the appearance of localized intracellular zones of clustered MNPs under the magnet is associated with extensive localized concentration of MNPs near cellular membranes and organelles or molecular markers. Magnet-induced NP clustering can be accompanied by shifts in PT-PA spectra that can be used to spectrally switch MNPs.

In the NIR range, MNPs exhibit significantly lower ($\geq$10-fold) PT and PA contrast than gold-based NPs [38]. Just as gold NPs coated with a dense layer of polymer [41] or silica [40] linearly enhanced PA signals, silica-coated MNPs (siMNPs) can also provide up to 5–10-fold greater linear amplification of PA-PT signals at low laser energy levels than simple MNPs; at higher laser energy levels, nonlinear amplification of PA-PT signals shows a large (so-called "giant") increase (20–35-fold) [38]. Spectral switching can also be achieved with MNPs by the contrast between the nonlinear amplification of PA spectra induced at shorter wavelengths and the stronger absorption by MNPs and the still linear PA effects induced at longer wavelengths with lower absorption by MNPs [38].

2.1.4 Photothermally induced nanobubbles as PA signal amplifiers and switching enhancers

Laser-induced nano- and microbubbles around overheated absorbing zones can play the role of giant (50–100-fold) PA signal amplifiers and PT therapy enhancers [26, 28, 35]. In addition, nanobubble-based amplification of PT and PA signals can enable novel nonlinear PT and PA imaging, in which spatial sharpening of PT and PA image structures can be achieved through signal enhancement around strongly absorbing zones, with the simultaneous potential for PT switching. Using similar phenomena, we recently pioneered super-resolution spectral PT and PA microscopy beyond the diffraction and spectral limits (i.e., PT and PA nanoscopy) for either label-free study of cellular nanostructures or NP clusters and PT/PA spectral burning techniques [28, 45, 46, 66]. Moreover, magnet-induced signal amplification (see above) can be associated with enhanced clustering of MNPs, whose overheating due to increased localized absorption upon laser irradiation can generate nanobubbles that act as PT and PA signal amplifiers [36, 38].

Laser-induced nanobubbles around plasmonic NPs lead to dramatic changes in the refraction index around the surfaces of NPs, which can be accompanied by a red shift in NP absorption in the range of 10–30 nm and hence in their PA and PT spectra [31, 39]. These phenomena can be used for dynamic spectral switching of NPs with the use of PT and PA effects to control the switching.

2.1.5 Switching of ultrasharp PT and PA resonances

The switching capability of existing NPs, especially plasmonic NPs, is limited by their wide (50–200 nm) NIR spectral bands, whose spectral overlapping may decrease PA contrast between unswitched and switched NPs. The recent discovery of ultrasharp nonlinear PA and PT resonances in various absorbing structures [28, 44, 45] can be used to dramatically enhance PT-based switching efficiency through the sharpening of spectral bands. The mechanism of these resonances is associated with laser-induced nonlinear amplification (10–100-fold) of PT and PA signals at specific wavelengths near the linear and nonlinear absorption maxima. Nonlinear effects may be related to absorption saturation, two- and multi-photon absorption, nonlinear scattering, interband transition, or generation of the second and third harmonics [28, 45, 50, 56–60]. Increased absorption of energy at specific laser wavelengths accompanied by the generation of nanobubbles with well defined thresholds only near these wavelengths leads simultaneously to amplification and spectral sharpening of PT and PA resonances [28]. These 1–4-nm-wide resonances can be observed both in the centers of linear plasmonic resonances and outside these centers at off-resonance laser wavelengths [28, 45]. Thus, dynamic nonlinear phenomena of PT and even non-PT origins (e.g., optical breakdown, ionization or Coulomb explosion [30]) at appropriate laser parameters (e.g., energy, pulse width, wavelength, and line

width) can dramatically amplify even small spectral peaks (not visible with conventional spectrophotometric techniques) in absorption spectra associated with plasmonic and Fano-resonances, surface-enhanced-resonance scattering (SERS), and nonlinear optical phenomena mentioned above. The detection methods can be based on time-resolved monitoring of nanobubble-related changes in the refractive index (which is important for PT and scattering methods) and strong acoustic waves (i.e., PA effect) [28]. More profound sharpening up to 0.8–1 nm in width can be observed in plasmonic NPs (GNRs and GNTs), while PT and PA resonance widths for other objects (e.g., proteins) can be broader, in the range of 4–10 nm. These phenomena can significantly increase spectral resolution and thus improve PT switching of multiple plasmonic NPs with precise control of small spectral shifts (up to a few nanometers) due to the narrow width of ultrasharp resonances (Figure 1B).

2.2 Schematic of integrated multimodal microscope

Photoswitching was tested with integrated PT and PA microscope techniques described elsewhere [43, 45, 46]. Briefly, this setup was built on the technical platform of an Olympus IX81 microscope (Figure 2) and a tunable optical parametric oscillator (OPO) with the following parameters: spectral range, 400–2,200 nm; pulse width, 5 nsec; pulse repetition rate, 100 Hz; and energy fluence range, $0.1–10^4$ mJ/cm^2. In PT thermal-lens mode, pump laser (OPO)-induced temperature-dependent variations of the refractive index cause defocusing of an unfocused collinear He–Ne laser probe beam (633 nm, 1.4 mW) and hence a reduction in the beam's intensity at its center. This is detected by a photodiode with a pinhole. Typical PT signals from the photodiode demonstrate an initial peak associated with rapid, picosecond-scale heating of cellular chromophores or NPs and with a slower, nano- to microsecond-scale exponential tail corresponding to the target's cooling. In nonlinear mode, laser-induced nanobubbles around overheating NPs leads to the appearance of sharp negative peaks associated with refraction and scattering of the probe beam on the nanobubbles (Figure 2, upper right). In the confocal schematic [46], the plane of the pinhole is fixed one Rayleigh distance from the probe-beam waist. PT images are constructed by acquiring PT signals from a sample as it undergoes scanning in x–y dimensions. For 3-D imaging, successive PT images are acquired in parallel x–y planes distributed along the z axis. Resolution in linear mode is determined by the microscope objective itself (e.g., ~0.7 μm at 20×, NA 0.4; and ~250 nm at 100×, NA 1.25). Resolution in nonlinear mode in the range of 50–120 nm depends on laser-induced nanobubble phenomena [66]. In PA mode, PA signals from the ultrasound transducer (an unfocused XMS-310 with 10 MHz frequency band, or a focused V316-SM with 20 MHz frequency band; both from Panametrics-NDT/Olympus) and amplifier (model 5662 or 5678, Panametrics) are recorded with the use of customized software. Fluorescence imaging, added to verify PT and PA data, is performed with a cooled color CCD camera (DP72, Olympus). Navigation of the laser beams for the *in vitro* study is controlled with a high-resolution (~300 nm) transmission digital microscopy module.

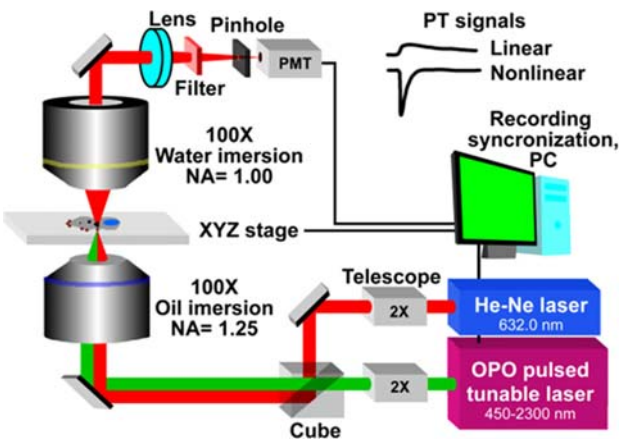

Figure 2 Schematic of the PT microscope.

2.3 Schematics of in vivo two-color photoswitchable PA flow cytometry (PAFC)

The principle and main components of PAFC have been described elsewhere [44]. Briefly, laser-induced PA waves from individual cells or NPs in blood flow are detected with an ultrasound transducer attached

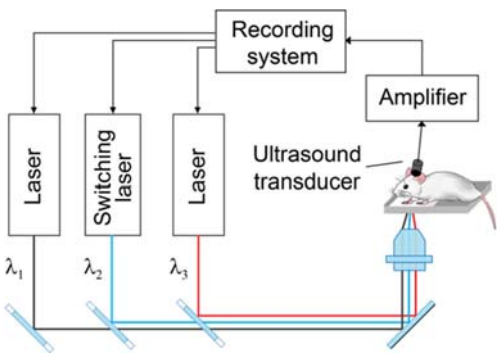

Figure 3 Schematic of the two-color (671/820 nm) PA flow cytometer.

to the skin above vessels (Figure 3). The PAFC setup was built on the platform of an Olympus BX51 inverted microscope that incorporated two high-pulse-rate lasers: 1) wavelength, 671 nm; pulse energy, 35 μJ; pulse width, 25 nsec; and repetition rate, up to 100 kHz (model: QL671-500, CrystaLaser); and 2) 820 nm; 75 μJ, 8 nsec, and 30 kHz (model: LUCE 820, Bright Solutions). In most applications of PAFC we used a 10 kHz pulse rate. The time delay (25 μs) between pulses with different wavelenghts provided real-time two-color detection of PA signals from the same cells using one ultrasound transducer [35]. Laser radiation is delivered to samples with the use of a customized condenser to create linear beam shapes whose dimensions could be adjusted from 10×50 μm to 25×100 μm by positioning the axial condenser. The PA signals have a bipolar shape with a typical duration of 0.1–1 μsec. They are usually transformed into a short pulse train because of the reflection and resonance effects in the transducer holder. PA signals are detected by ultrasound transducers (described above) and then amplified (amplifier model 5662: bandwidth, 50 kHz–5 MHz; gain, 54 dB; and model 5678: 40 MHz and 60 dB; both from Panametrics). To collect PA signals, the PAFC setup is equipped with a high-speed, analog-to-digital converter board. In analogy to conventional flow cytometry, final PA data are presented as PA signal traces that are analyzed with customized software.

2.4 PSFPs in vitro and in mammalian cells

Recombinant PSFPs, such as Dendra2, PSmOrange, and PSmOrange2, were expressed in bacteria and purified as previously described [14]. The obtained PSFP stock solution in phosphate-buffered saline (PBS) was diluted with PBS to 3 μM, which approximately corresponded to its concentration in the cytoplasm of stably expressing mammalian cells. The solution was mixed with inert optical transparent oil and rigorously shaken to prepare small drops of PSFPs, which were placed on slides for further studies.

Rat MTLn3 adenocarcinoma cells, originally isolated by Neri and Nicolson (Institute for Molecular Medicine), were maintained in minimum essential medium á (Life Technologies) with 5% fetal bovine serum and penicillin – streptomycin (Life Technologies). A preclonal mixture of MTLn3 expressing Dendra2 was used in all experiments. Viable cells were resuspended in PBS and placed into a 120-μm-thick well attached to the glass slide. MDA-MB-231 human breast cancer cells (American Type Culture Collection) were cultured according to the vendor's specifications. The cells were cultured to confluency *in vitro,* detached with 0.25% trypsin–0.53 mM EDTA solution, washed, resuspended in PBS, and then used for *in vitro* studies. The viability of cells was >98.5% according to the trypan blue exclusion test.

Dendra2 photoswitching in solution and in live mammalian cells was performed with a 405 nm diode laser, and PSmOrange and PSmOrange2 were photoswitched with a 488 nm laser. A focused laser beam was used to photoswitch individual cells. For photoswitching of a large number of cells in suspension in a cuvette (1.5 mL, 5×10^6 cells), the laser spot was defocused by a ground-glass diffuser, resulting in a 15 mm beam diameter that was comparable to the size of the cuvette. In some comparative tests, PSFP solutions were photoswitched with a mercury lamp with the use of the respective excitation filters.

2.5 Animal models

Animals were used in accordance with a protocol approved by the University of Arkansas for Medical Sciences (UAMS) Institutional Animal Care and Use Committee (IACUC). Nude mice (*nu/nu*), 8–10 weeks old, weighing 20–30 g, were procured from a commercial source for use in the experiments. The animals were anesthetized by isoflurane and placed on a heated microscope stage (at 38 °C [body temperature]) [44].

2.6 Nanoparticles

GNRs having maximum absorption at 820 nm were conjugated with antibodies specific to leukocyte receptor CD45 (Nanopartz). Spherical MNPs (Ocean NanoTech) measuring 30 nm were used as triple-modal (magnetic, PT, and PA) contrast agents. The plasmonic MNPs consisting of a 15 nm iron-oxide spherical core were covered by 2 nm gold shells. Iron oxide NPs were synthesized by using a seed-mediated oxido-reduction reaction between the iron salt $FeCl_3$ (0.16 mmol) and the reduction agent, $NaBH_4$. A mixture of 3 : 1 oleylamine and oleic acid was used as a capping agent, and 100 μL of $AgCl_2$ (0.01 M) were used as seeds. After the addition of $NaBH_4$, the color of the pale yellow solution immediately changed to black. The black mixture was stirred overnight to stabilize the formed iron-oxide NPs. The NPs were then purified by washing them several times with ethanol and hexane. To create the gold layer around the iron-oxide NPs, a molar ratio of 1 : 200 iron-oxide NPs to gold salt in hexane was used with oleylamine as a reduction and capping agent. The core-shell MNPs were precipitated with ethanol, capped with a magnet, and washed several times with hexane and chloroform. Finally, 5 mg of core-shell NPs were re-

dispersed in 0.5 mL of 0.1 mM hexa decyltrimethyl ammonium bromide (CTAB).

A permanent magnetic field was provided for manipulating MNPs with a cylindrical neodymium-iron-boron (NdFeB) magnet with a Ni–Cu–Ni coating, measuring 3.2 mm in diameter and 9.5 mm long and having a surface field strength of 0.39 Tesla (MAGCRAFT). The magnetic tip was attached to the top cover of the slides containing the MNP-labeled cancer cell suspension. To target breast cancer cells with overexpressed CD44 receptors, MNPs were conjugated with antibodies (Abs) specific to the human CD44 receptor. After a 10 min incubation with NPs at 23 °C and centrifugation at 10,000 g for 5 min, the residual Abs were removed by washing three times with 10 mM PBS, pH 8.2, containing 1% bovine serum albumin The conjugation was verified by PT microscopy [36]. The cells were incubated with MNP–CD44 conjugates for 1 h at 37 °C. The necessary concentration of NPs was calculated on the basis of our previous data: 10^2–10^3 NPs per cell [36, 44]. Subsequently, labeled cells were resuspended in PBS and placed in 8.6 μL wells (Molecular Probes).

2.7 Transmission electron microscopy (TEM)

TEM was used to visualize the NPs as prepared. Iron oxide-covered gold-shell NPs in a volume of 20 μL were deposited onto the 300 mesh carbon-coated Cu grid. The TEM images were acquired with a JEOL JEM microscope at an accelerating voltage of 80 kV. ImageJ software was used to measure the diameters of NPs used.

3. Results

The phenomenological model of photoswitchable PT and PA probes presented above was verified with MNPs and GNRs. We also tested the capability of PT and PA microscopy to control conventional photoswitching of PSFPs by monitoring their switching in absorption and comparing these data with PT switching of PTSNs.

3.1 In vitro integrated PT-magnetic switching of cancer cells labeled with functionalized MNPs

We explored the mechanisms of reversible PT-magnetic switching based on magnet-induced clustering

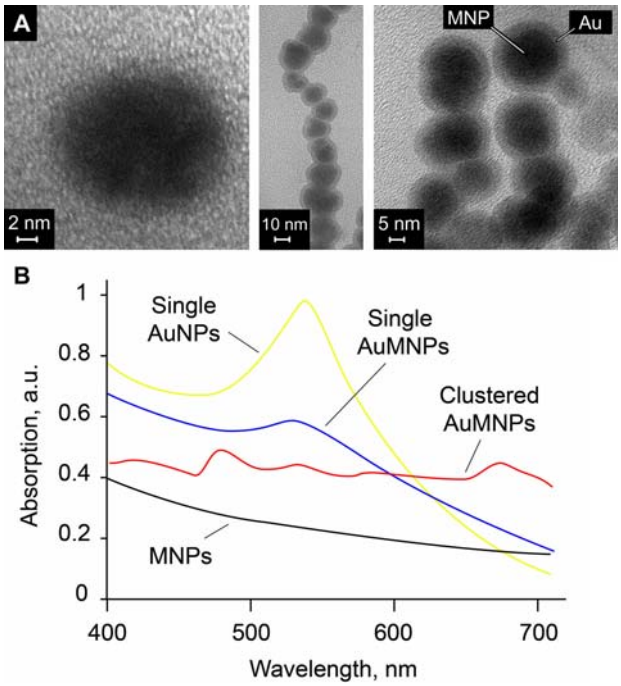

Figure 4 Magnetic nanoparticles. (**A**) TEM images of 15 nm magnetic nanoparticles (MNPs) coated with 2 nm gold shell: single (left), chained (middle), and clustered (right) gold-coated MNPs. (**B**) Absorption spectra of single and clustered gold, magnetic, and gold-coated MNPs. Spectra were normalized at maximal absorption of single gold NPs at a wavelength of 530 nm. The total amounts of various NPs in solution were similar.

of conventional MNPs and plasmonic gold-coated MNPs (AuMNPs) (Figure 4) in individual cells, followed by PT disintegration of the NP clusters. Specifically, the cells were incubated with both types of NPs and labeled molecularly or by endocytosis (2 h at 37 °C). Both demonstrated similar magnetic-PT switching phenomena (see details below). Conventional MNPs exhibited intrinsic absorption at short visible wavelengths that monotonically decreased through the visible into the NIR ranges (Figure 4B) [35, 38]. The PT signals from AuMNPs at 532 nm were approximately 8–10 fold higher than those from conventional MNPs because of plasmonic-enhanced absorption (Figure 4B). In addition, the PT signal decrease at 532 nm was more profound during AuMNP clustering inside cells because of a red shift in the absorption spectrum (Figure 4B). However, magnetic-switching efficiency was lower during AuMNP clustering inside cells and required a long magnet exposure time (30 min), likely because of the weaker magnetic properties of AuMNPs. This issue requires further study.

We tested the magnetic-PT switching using an OPO system (Figure 2) at two wavelengths, 532 nm and 671 nm. Before switching, the laser energy flu-

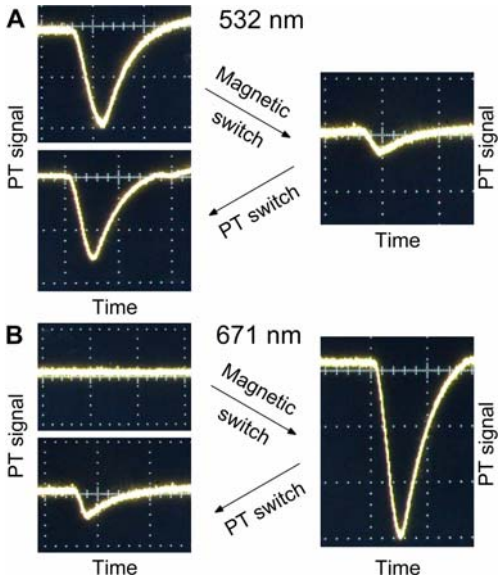

Figure 5 Reversible magnetic-PT switching of MNPs in cancer cells. Nonlinear PT signals from individual breast cancer cells (MDA-MB-231) with MNPs at laser wavelengths of 532 nm (**A**) and 671 nm (**B**) before and after magnetic switching by cell exposure to a magnet (10 min), and then after PT switching using a single laser pulse at an increased energy fluence (0.5 J/cm^2, 532 nm). Laser pulse energy fluence in diagnostic mode: 50 mJ/cm^2 at 532 nm and 100 mJ/cm^2 at 671 nm. Amplitude and time scale: 50 mV/div and 2 μsec/div.

ence was adjusted so that single cells incubated with MNP–CD44 conjugates produced PT signals at 532 nm (Figure 5A top, left) and no signals at 671 nm (Figure 5B, top, left). Attachment of a magnetic tip to the top cover of the slide containing cells labeled by MNP–CD44 for 10 min led to cells concentrating around the area of the magnet, as we had observed in previous studies [36]. This phenomenon was accompanied by a slight decrease in PT signals at 532 nm (Figure 5A, right) and the appearance of strong PT signals at 671 nm (Figure 5B, right). Exposure of the cell to a single laser pulse at 532 nm at a relatively high energy level led to the recovery of PT signals at 532 nm almost to the initial level (Figure 5A, bottom, left), while the PT signals at 671 nm dramatically decreased (Figure 5B, bottom, left).

According to our phenomenological model (Section 2.1.3), the observed phenomena could be explained by magnet-induced MNP clustering [36] that led to increased localized absorption with the generation of nanobubbles around overheated clusters as a powerful PT-signal amplifier [35] at 671 nm; in contrast, nanobubbles were absent around MNPs that were not clustered. Surprisingly, after magnetic action, we observed a decrease in PT signals at 532 nm. This can be explained by a slight decrease in localized absorption with less effective nanobubble formation. Irradiation of cells after magnetic action at a relatively high pulse energy level most likely led to nanobubble-induced MNP cluster disintegration, as we had previously observed with conventional gold nanosphere clusters [29]. Thus, magnetic action led to notable enhancement in PT signals at 671 nm within one cell, while the laser pulse at a relatively high energy level provided reversible PT-based switching to almost that of the previous MNP state. The low-level signal remaining at 671 nm was probably associated with small MNP clusters that were not completely disintegrated during PT switching. Nevertheless, these results demonstrate the feasibility of magnetic and PT switching with conventional MNPs.

3.2 In vivo PT switching of functionalized gold NPs in single circulating cells

We explored the mechanism of switching based on laser-induced modifications of GNR shapes and sizes accompanied by a blue shift in NP absorption spectra. We tested this approach using two-color PAFC (671 nm/820 nm) (Figure 3). The principle of PT switching using spatially separated laser beams is shown in Figure 6. Cells labeled with unswitched GNRs having a plasmonic resonance near 820 nm first crossed an 820-nm-wavelength laser beam, which resulted in the generation of high-amplitude PA signals (Figure 6A). The cells then crossed an NIR laser, which photoswitched the GNRs from absorption at 820 nm to absorption at 671 nm. Finally, the cells with switched GNRs crossing the 671 nm laser generated preferentially relatively high-amplitude PA signals at 671 nm. To photoswitch GNRs, a

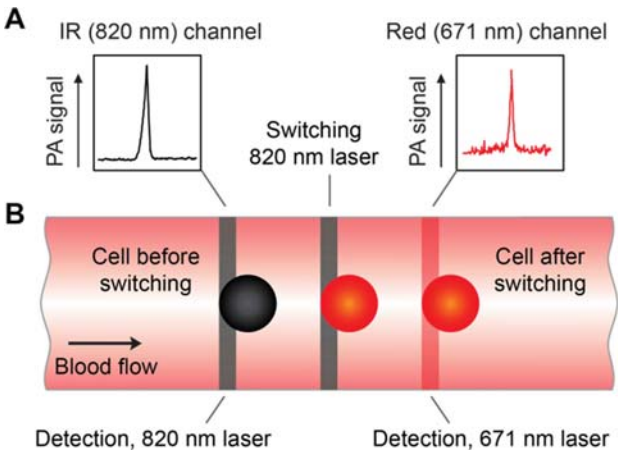

Figure 6 Principle of PT switching of plasmonic nanoprobes targeted to circulating cells. (**A**) PA signals in infrared (IR) and red detection channels from unswitched and switched nanoprobes, respectively. (**B**) Photoswitching of nanoprobes in cells directly in the bloodstream.

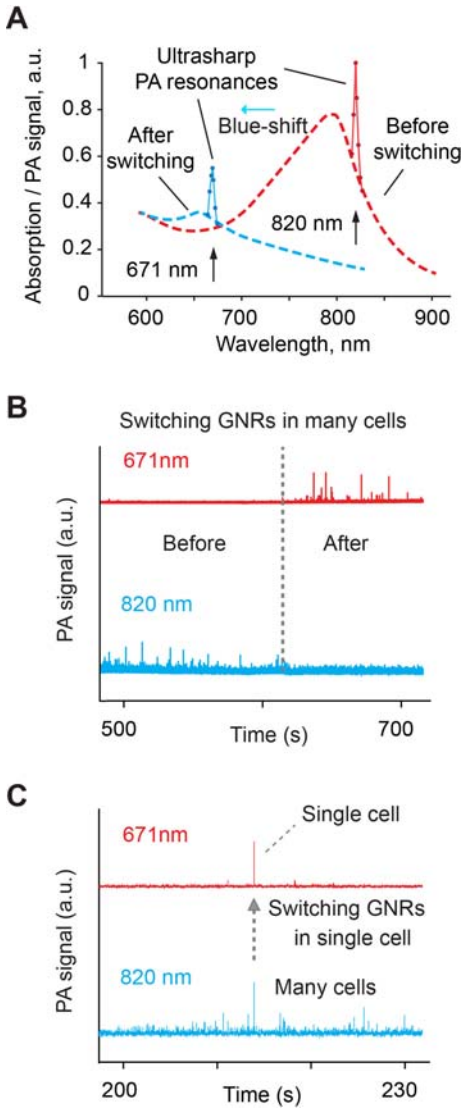

Figure 7 PT switching of plasmonic nanoprobes *in vivo* in blood flow. (**A**) Absorption spectra and ultrasharp PA resonances in gold nanorods (GNRs) *in vitro* before and after PT switching. Two-color (671/820 nm) PA monitoring of PT switching of GNRs in many (**B**) and single (**C**) white blood cells.

relatively high-pulse-energy laser beam can be focused on a blood vessel between two low-pulse laser beams used to detect CTCs before and after PT switching (Figure 6B). This laser array with one ultrasound transducer and two recording channels [35] can (1) detect a signal from a single cell with the initial plasmonic absorption of GNRs by using the first laser at 820 nm, (2) photoswitch GNRs in a cell passing through the second laser, and (3) detect a signal from the cell with PT-switched, blue-shifted GNR absorption with the third laser. Analysis of signal amplitudes, widths, and rates may provide information on size, velocity [44], and number of cells with initial and switched GNRs. In other words, the efficiently switched GNRs exhibited two subsequent signals of similar amplitude on the signal-trace records: first a signal at 820 nm and then a signal at 671 nm. The laser beams with different wavelengths can spatially overlap, and a laser with the same wavelength (e.g., 820 nm) can be used for both PA detection at low energy and PT switching at higher energy, as described below.

This phenomenological model was tested with GNRs with a maximum absorption at 820 nm (GNR_{820}) (Figure 7A) and conjugated with antibodies specific to the leukocyte (white blood cell [WBC]) receptor CD45 [44]. The solution of GNR_{820}–CD45 conjugates at an NP concentration of 10^{12}/mL was intravenously injected in a volume of 50 μL into an intact nude mouse; two-color (671 nm/820 nm) PA monitoring of blood microvessels in the mouse ear followed. After successfully targeting the WBCs over a period of 20–30 min (see [44] for details of cell labeling in blood flow), we observed PA signals preferentially at 820 nm, using a relatively low laser energy fluence (15 mJ/cm^2) at 820 nm. When we applied a relatively high laser energy at 820 nm (PT switching), the PA signal level decreased at 820 nm (Figure 7B), and immediately we observed PA signals at 671 nm that were absent before PT switching. We also revealed that a short laser exposure (10 msec) at a high energy level at 820 nm resulted in successfully photoswitching only one cell to the 671 nm range (Figure 7C). Further, we confirmed a blue shift in GNRs *in vitro* when we compared the absorption and PA spectra of GNR_{820}–CD45-labeled cells before and after laser exposure at 820 nm at an energy fluence of 100 mJ/cm^2 (Figure 7A). These effects are related to highly localized PT heating of GNRs accompanied by the known transformation of GNRs from rod to ellipsoid with an absorption maximum at shorter wavelengths [32–33]. The indicated laser energy fluences at the selected wavelengths (820 nm and 671 nm) were adjusted to provide energy-dependent ultrasharp PA spectra resonances measuring 2–4 nm wide (see details in section 2.1.5 [28]).

3.3 Photoswitchable fluorescent proteins as triple-modal (fluorescent, PT, and PA) contrast agents

In Section 3.2, we demonstrated, for the first time, successful PT switching of plasmonic gold NPs (GNRs) as high-contrast PT and PA agents. For comparison, we tested the capability of a PT microscope integrated with a fluorescence imaging module (Figure 2 [46]) to control switching in conventional PSFPs, in which the photoswitching mechanism is as-

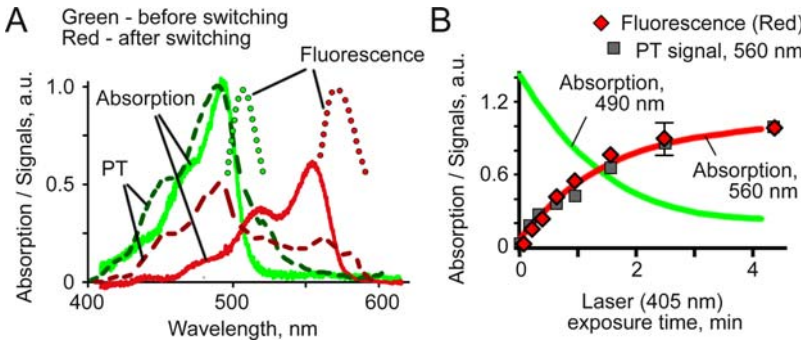

Figure 8 Photoswitchable fluorescent proteins as triple-modal (fluorescent, PT, and PA) contrast agents. (**A**) Absorption (solid curves), PT (dashed curves), and fluorescence (dotted curves) spectra of purified Dendra2 before (green) and after (red) photoswitching with a 405 nm laser. (**B**) Temporal monitoring of photoswitching of purified Dendra2 with absorption, PT, and fluorescence methods during exposure to a 405 nm laser.

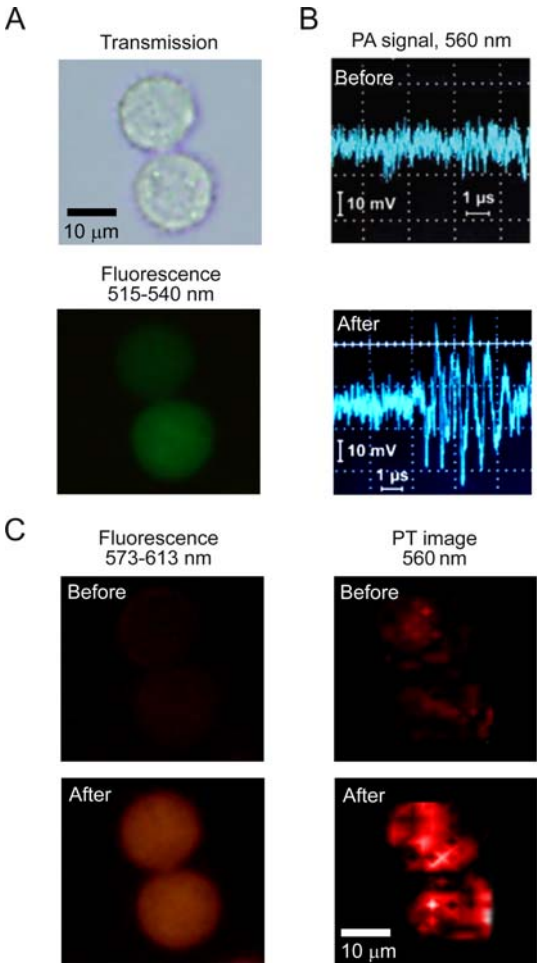

Figure 9 Images and PA signals from cancer cells labeled with photoswitchable fluorescent proteins. (**A**) Transmission (top) and fluorescence images of single MTLn3 cells with Dendra2 in green channel (bottom) before photoswitching. (**B**) PA signals from the same single cells at wavelength of 560 nm before (top) and after (bottom) photoswitching. (**C**) Flourescence image of the same cells in red channel (left) and PT image (right) before (top) and after (bottom) photoswitching.

sociated with photochemical processes induced by exposure to laser radiation [14].

For possible use with PT-PA techniques, we tested three PSFPs – Dendra2, PSmOrange, and PSmOrange2 – using a conventional arc lamp with a filter and lasers at wavelengths of 405 nm and 488 nm to photoswitch Dendra2 and the PSmOranges, respectively. We chose Dendra2 for further study because it provided the fastest, most efficient photoswitching and stronger PT and PA signals. Thus, although Dendra2 has a relatively high quantum yield (~50% before and ~55% after photoconversion), approximately one-half of the absorbed laser energy is converted into heat that can be detected with PT or PA techniques. Indeed, the high sensitivity of PT and PA techniques enables measuring Dendra2's absorption spectra before and after photoswitching in solution (Figure 8) and in individual labeled cells (Figure 9). Specifically, increasing the light exposure at 405 nm to 11 mW led to photoswitching of the maximum absorption of Dendra2 from 490 nm to 560 nm and the corresponding maximum emission from 525 nm to 580 nm (Figure 8A), accompanied by increases in both fluorescence intensity and the PT signal amplitudes that were significantly correlated with each other (Figure 8B). PT imaging provided relatively good-contrast PT images of single MTLn3 tumor cells expressing Dendra2 at 560 nm after photoswitching (Figure 9C, bottom, right). The PT images revealed the spatial heterogeneity of Dendra2's distribution in the cellular cytoplasm, which may serve as an indicator of the presence of highly localized Dendra2 - molecule nanoclusters that amplify PT signals [24, 29, 46]. In contrast, fluorescence images of the same cells could not distinguish these heterogeneities (Figure 9C, bottom, left). PA technique also demonstrated the capability to detect single cells with photoswitched Dendra2 *in vitro* (Figure 9B, bottom). However, we encountered a problem with the PA detection of circulating single cells with PSFPs *in vivo* in small ear microvessels because of the relatively low

absorption of Dendra2 against the background absorption of blood; using PSFPs with absorption at wavelengths >620 nm should improve this situation.

4. Discussion

We introduce a new concept of spectrally photoswitchable PT and PA nanoprobes (PTSNs) with a focus on PT switching of plasmonic nanoprobes and combined magnetic–PT switching of NPs with magnetic properties. PTSNs offer many potential advantages over conventional PSFPs including a much faster PT-switching time (nanoseconds vs. 0.1–10 sec), much higher PT and PA contrast (10–100-fold), lower toxicity, and operation in the NIR spectral window of tissue transparency. Nevertheless, we have shown that PT and PA techniques may provide the ability to control conventional photoswitching of PSFPs (e.g., Dendra2) at the single-cell level. We believe that the integration of PT-PA and fluorescence microscopy, especially using two laser beams for excitation of both fluorescence and PT-PA signals from PSFPs, could be feasible. Thus, use of the same laser in both methods may increase the total number of PSFPs with different absorption and fluorescence properties, especially with a low quantum yield.

Nevertheless, to increase the sensitivity and resolution of PT-PA techniques, we proposed alternative mechanisms based on known modifications in the shape of GNRs accompanied by a blue shift in GNR absorption spectra under NIR laser exposure, and on magnetic-induced MNP aggregation/clustering followed by PT-induced MNP disaggregation. These phenomena were first observed with the use of conventional gold nanosphere clusters [29, 45], which are nontoxic, simpler to synthesize, more stable, and less expensive than other NPs. Thus, gold and magnetic nanospheres and gold–magnetic hybrids could be good choices for PT switching using nanobubble-induced signal amplification. It is important to emphasize that nanobubble formation can be controlled before, during, and after NP modification (e.g., melting) by selection of the proper laser parameters, such as laser pulse fluence and duration [39]. Indeed, high laser energy levels and strong NP absorption can rapidly heat NPs during laser pulses, even at the beginning of the pulse, leading to modification of NP shapes and sizes and hence to controllable change of spatially specific, nanoscale absorption properties that can amplify PT and PA effects. These phenomena are relatively universal and can be observed with different single and clustered NPs, including gold nanospheres, quantum dots, GNTs, GNSs, GNRs, and MNPs.

These and other PTSNs may have a broad spectrum of potential biological applications similar to those of PSFPs [3–14], but with the ability to assess nonfluorescent structures in a single cell *in vivo*. In addition, PTSNs can be used to photoswitch and track individual cells. We demonstrated this approach using two-color (671 nm/820 nm) *in vivo* PAFC by PA monitoring of circulating cells targeted directly in the bloodstream. This technique, due to its high sensitivity, can be important for detecting CTCs, as we demonstrated in melanoma and breast cancer models [35, 37]. Indeed, despite substantial efforts to understand the biology of metastases, which cause up to 90% of cancer deaths, the mechanisms of metastasis are still poorly understood [61–65]. Comprehensive studies have shown the potential of using CTC counts as a marker of metastasis development, cancer recurrence, and therapeutic efficacy [64]. Nevertheless, knowledge of how CTCs disseminate through the body and cause primary and secondary metastases (so-called metastasis cascade model) is limited. For example, current detection and imaging techniques using conventional labeling are not suitable for identifying the origin of CTCs (i.e., from primary tumor or from metastases), as all seeding cells (new seeds, reseeds, and self-seeds [65]) have the same label color. This principal limitation also restricts our ability to identify tumor-initiating or cancer stem cell tracks [64]. We are confident that the PAFC system using the new PTSNs has the potential in the future to provide insights into these processes. By rapidly (picosecond–nanosecond scale) photoswitching PTSNs in targeted cells directly in the circulation with a single short laser pulse, we can potentially mark individual CTCs and then monitor their further dissemination. This capability also allows studying cell traffic in the circulation under normal and pathological conditions. In addition, breast CTCs can be magnetically enriched in the circulation with MNPs conjugated with ligands specific to folate and a urokinase-type plasminogen activator receptor of CTCs [35]. A similar approach is applicable for tagging breast cancer stem cells [36], melanoma cells [37], and *Staphylococcus aureus* [38] using CD44, melanoma-associated chondroitin sulfate proteoglycan, and staphylococcal protein A (or lipoprotein) receptors. CTCs targeted by MNPs can be magnetically captured in flow at velocities up to 5–10 cm/sec and in vessels of up to 1–2 mm in diameter by using a magnet with a field strength of 0.4–0.7 Tesla [35]. A fiber-based PA–magnet probe can also provide the opportunity for PA- (or PT)-guided magnetic manipulation of MNPs in cells [36, 38].

In conclusion, using light to control the spectral properties of metal and particularly gold NPs or aggregations of NPs is not completely new [47–58]. However, the engineering of nonfluorescent absorbing PTSNs with controllable spectral shifts in absorption in response to laser radiation is challenging. Most existing contrast agents, especially NPs, are not quite optimal for this purpose because their absorption

spectra are too broad, they exhibit small spectral shifts, or their photoconvertion is too slow. In addition, contrast-agent aggregation is often uncontrollable in a biological environment, and multicolor and multiplex capacity is limited. For example, previous attempts in which NPs were doped in SiO_2-TiO_2 matrix or coated with photosensitive polymers (e.g., photo-trans-*cis*-isomerization of chromophores) were limited by their operation in the UV- and visible-spectral ranges, the small magnitude of photo-induced spectral effects, a lengthy light exposure time [53], and film-associated conditions. These approaches have also never been applied in PT-PA techniques. We presented an advanced platform and described new approaches for engineering PTSNs that can provide a new class of multicolor PT and PA contrast nanoagents capable of ultrafast, temporally and spatially selective spectral shifts (up to 50–200 nm) in the NIR absorption spectrum in response to short laser pulses and potentially to a strong magnetic field. As mentioned previously, spectral selectivity for identifying multiple disease (e.g., cancer) markers is limited by the wide NIR spectral band (80–150 nm) of most NPs (e.g., GNRs, GNSs) that allows the effective use of only two nonoverlapping colors. To target multiple markers, multicolor PTSNs (at least four to eight colors) with ultrasharp nonlinear PA and PT resonances in plasmonic NPs with spectral widths up to 1–4 nm [28, 45] can be used now for both PA diagnosis and PT therapy. Using similar nonlinear phenomena with conventional contrast agents, we demonstrated super-resolution spectral PT and PA microscopy beyond diffraction and spectral limits [28, 45, 46, 66]. We believe that photoswitchable proteins and especially new PTNPs can be used in super-resolution PT and PA imaging in analogy to fluorescence STORM and PALM schematics [1]. For example, switching of a PT and PA contrast agents within diffraction spots will allow achieving a resolution of 10–20 nm compared to current 50–100 nm [66].

Acknowledgements This work was supported by NIH grants EB000873, CA131164, EB009230, and CA139373 and by Department of Defense grants W88XWH-10-2-0130, W81XWH-10-BCRP-CA, and W81XWH-11-1-0129. We thank Dr. Watanabe for collecting the TEM images of NPs used in this manuscript.

Author biographies Please see Supporting Information online.

References

[1] C. G. Galbraith and J. A. Galbraith, J. Cell Sci. **124,** 1607–1611 (2011).
[2] N. C. Shaner, G. H. Patterson, and M. W. Davidson, J. Cell Sci. **120**, 4247–4260 (2007).
[3] K. Hatta, H. Tsuji, and T. Omura, Nat Protocols **1**, 960–967 (2006).
[4] J. N. Henderson, H. W. Ai, R. E. Campbell, and S. J. Remington, Proc. Natl. Acad. Sci. USA **104**, 6672–6677 (2007).
[5] S. Habuchi, H. Tsutsui, A. B. Kochaniak, A. Miyawaki, and A. M. van Oijen, PLoS One **3**, e3944 (2008).
[6] V. Adam, K. Nienhaus, D. Bourgeois, and G. U. Nienhaus, Biochemistry **48**, 4905–4915 (2009).
[7] S. A. McKinney, C. S. Murphy, K. L. Hazelwood, M. W. Davidson, and L .L. Looger, Nat. Methods **6**, 131–133 (2009).
[8] B. Huang, M. Bates, and X. Zhuang, Annu. Rev. Biochem. **78**, 993–1016 (2009).
[9] G. Hamer, O. Matilainen, and C. I. Holmberg, Nat. Methods **7**, 567 (2010).
[10] S. M. Baker, R. W. Buckheit 3rd, and M. M. Falk, BMC Cell Biol. **11**, 15 (2010).
[11] H. Hoi, N. C. Shaner, M. W. Davidson, C. W. Cairo, J. Wang, and R. E. Campbell, J. Mol. Biol. **401**, 776–791 (2010).
[12] K. I. Willig, A. C. Stiel, T. Brakemann, S. Jakobs, and S .W. Hell, Nano Lett. **11**, 3970–3973 (2011).
[13] V. Adam, B. Moeyaert, C. C. David, H. Mizuno, M. Lelimousin, P. Dedecker, R. Ando, A. Miyawaki, J. Michiels, Y. Engelborghs, and J. Hofkens, Chem. Biol. **18**, 1241–1251 (2011).
[14] O. M. Subach, G. H. Patterson, L. M. Ting, Y. Wang, J. S. Condeelis, and V. V. Verkhusha, Nat. Methods **8**, 771–777 (2011).
[15] O. M. Subach, D. Entenberg, J. S. Condeelis, and V. V. Verkhusha, J. Am. Chem. Soc. **134**, 14789–14799 (2012).
[16] E. H. Rego, L. Shao, J. J. Macklin, L. Winoto, G. A. Johansson, N. Kamps-Hughes, M. W. Davidson, and M. G. Gustafsson, Proc. Natl. Acad. Sci. USA **109**, E135–E143 (2012).
[17] Y. T. Kao, X. Zhu, and W. Min, Proc. Natl. Acad. Sci. USA **109**, 3220–3225 (2012).
[18] D. Rasansky, M. Distel, C. Vinegoni, R. Ma, N. Perrimon, R. W. Koster, and V. Ntziachristos, Nat. Photonics **3**, 412–417 (2009).
[19] L. V. Wang, Nat. Photonics **3**, 503–509 (2009).
[20] Y. Y. Petrov, I. Y. Petrova, I. A. Patrikeev, R. O. Esenaliev, and D. S. Prough, Opt. Lett. **3**, 1827–1829 (2006).
[21] S. Ermilov, A. Stein, A. Conjusteau, R. Gharieb, R. Lacewell, T. Miller, S. Thompson, P. Otto, B. McCorvey, T. Khamapirad, M. Leonard, and A. Oraevsky, Proc. SPIE **6437**, 643703-1–643703-11 (2007).
[22] L. V. Wang and S. Hu, Science **335**, 1458–1462 (2012).
[23] S. Mallidi, G. P. Luke, and S. Emelianov, Trends Biotechnol. **29**, 213–221 (2011).
[24] J. W. Kim, E. I. Galanzha, E. V. Shashkov, H. M. Moon, and V. P. Zharov, Nat. Nanotechnol. **4**, 688–694 (2009).
[25] G. P. Luke, D. Yeager, and S. Y. Emelianov, Ann. Biomed. Eng. **40**, 422–437 (2012).

[26] A. de la Zerda, J. W. Kim, E. I. Galanzha, S. S. Gambhir, and V. P. Zharov, Wiley's Contrast Media Molec. Imaging J. **6**, 346–369 (2011).
[27] J. W. Kim, E. I. Galanzha, D. A. Zaharoff, R. J. Griffin, and V. P. Zharov, Mol. Pharmacol. **4,** 813–830 (2013).
[28] V. P. Zharov, Nat. Photonics **5**, 110–116 (2011).
[29] V. P. Zharov, E. N. Galitovskaya, C. Jonson, and T. Kelly, Laser Surg. Med. **37**, 219–226 (2005).
[30] R. R. Letfullin, C. Joenathan, T. F. George, and V. P. Zharov, J. Nanomed. **1**, 473–480 (2006).
[31] C. M. Aguirre, C. E. Moran, J. F. Young, and N. J. Halas, J. Phys. Chem. B **108**, 7040–7045 (2004).
[32] S. S. Chang, C. W. Shih, C. D. Chen, W. C. Lai, and C. R. C. Wang, Langmuir **15**, 701–709 (1999).
[33] S. Link, C. Burda, B. Nikoobakht, M. A. El-Sayed, J. Phys. Chem. B **104**, 6152–6163 (2000).
[34] G. Akchurin, B. Khlebtsov, G. Akchurin, V. Tuchin, N. Khlebtsov, and V. P. Zharov, Nanotechnology **19**, 015701 (2008).
[35] E. I. Galanzha, E. V. Shashkov, T. Kelly, J. W. Kim, L. Yang, and V. P. Zharov, Nat. Nanotechnol. **4**, 855–60 (2009).
[36] E. I. Galanzha, J. W. Kim, and V. P. Zharov, J. Biophotonics **2**, 725–735 (2009).
[37] D. Nedosekin, M. Sarimollaoglu, J. H. Ye, E. I. Galanzha, and V. P. Zharov, Cytometry **79A**, 825–833 (2011).
[38] E. I. Galanzha, E. Shashkov, M. Sarimollaoglu, K. E. Beenken, A. G. Basnakian, M. E. Shirtliff, J. W. Kim, M. S. Smeltzer, and V. P. Zharov, PLoS One **7**, e45557 (2012).
[39] V. Pustovalov, A. Smetannikov, and V. Zharov, Laser Phys. Lett. **5**, 775–792 (2008).
[40] Y. S. Chen, W. Frey, S. Kim, P. Kruizinga, K. Homan, and S. Emelianov, Nano Lett. **11**, 348–354 (2011).
[41] V. P. Zharov, E. I. Galanzha, E. V. Shashkov, J. W. Kim, N. G. Khlebtsov, and V. V. Tuchin, J. Biomed. Opt. **12**, 0551503 (2007).
[42] D. A. Nedosekin, E. V. Shashkov, E. I. Galanzha, L. Hennings, and V. P. Zharov, Cytometry A **77**, 1049–1058 (2010).
[43] M. V. Khodakovskaya, K. Silva, D. A. Nedosekin, E. Dervishi, A. B. Biris, E. V. Shashkov, E. I. Galanzha, and V. P. Zharov, Proc. Natl. Acad. Sci. USA **108**, 1028–33 (2011).
[44] E. I. Galanzha and V. P. Zharov, Methods **57**, 280–296 (2012).
[45] J. Shao, R. J. Griffin, E. I. Galanzha, J. W. Kim, N. Koonce, J. Webber, T. Mustafa, A. Biris, D. A. Nedosekin, and V. P. Zharov, Sci. Rep. **3**, 1293 (2013).
[46] D. A. Nedosekin, E. I. Galanzha, S. Ayyadevara, R. J. Shmookler Reis, and V. P. Zharov, Biophys. J. **102**, 672–681 (2012).
[47] M. S. Yavuz, G. C. Jensen, D. P. Penaloza, T. A. P. Seery, S. A. Pendergraph, J. F. Rusling, and G. A. Sotzing, Langmuir **25**, 13120–13124 (2009).
[48] J. Byun, J. Shin, S. Kwon, S. Jang, and J. K. Kim, Chem. Commun. **48**, 9278–9280 (2012).
[49] J. Baumgard, L. Humbert, E. Boulais, R. Lachaine, J. J. Lebrun, and M. Meunier, Biomaterials **33**, 2345–2350 (2012).
[50] X. Huang, W. Qian, I. H. El-Sayed, and M. A. El-Sayed, Lasers Surg. Med. **39**, 747–753 (2007).
[51] R. Klajn, K. J. M. Bishop, and B. A. Grzybowski, Proc. Natl. Acad. Sci. USA **104**, 10305–10309 (2007).
[52] N. Venkatram, R. S. S. Kumar, D. N. Rao, S. K. Medda, S. De, and G. De, J. Nanosci. Nanotechnol. **6**, 1990–1994 (2006).
[53] A. Housni, Y. Zhao, and Y. Zhao, Langmuir **26**, 12366–12370 (2012).
[54] A. J. Wagstaff, S. D. Brown, M. R. Holden, G. E. Craig, J. A. Plumb, R. E. Brown, N. Schreiter, W. Chrzanowski, and N. J. Wheate, Inorganica Chimica Acta **393**, 328–333 (2012).
[55] W. Liu, Y. Zhang, S. Ge, X. Song, J. Huang, M. Yan, and J. Yu, Anal. Chim. Acta **770**, 132–139 (2013)
[56] M. Hari, A. J. Santhi, B. Nithyaja, S. Matthew, R. Kumar, G. Mishra, R. R. Yadhav, P. Radhakrishnan, and V. P. N. Nampoori, J. Nonlinear. Optic Phys. Mater. **20**, 467–475 (2011).
[57] C. K. Lo, D. Xiao, and M. M. F. Choi, J. Mater. Chem. **17**, 2418–2427 (2007).
[58] D. Yelin, D. Oron, D. Thiberge, S. Moses, and Y. Silberberg, Opt. Express **11**, 1385–1391 (2003).
[59] J. Nappa, I. Russier-Antoine, E. Benichou, and P. F. Brevet, J. Chem. Phys. **125**, 184712 (2006).
[60] R. Antoine, P. F. Brevet, H. H. Girault, D. Bethellb, and D. J. Schiffrinb, Chem. Commun. **19**, 1901–1902 (1997).
[61] C. L. Chaffer and R. A. Weinberg, Science **331**, 1559–1564 (2011).
[62] J. E. Talmadge and I. J. Fidler, Cancer Res. **70**, 5649–5669 (2010).
[63] C. Alix-Panabières, H. Schwarzenbach, and K. Pantel, Annu. Rev. Med. **63**, 199–215 (2012).
[64] M. Yu, S. Stott, M. Toner, S. Maheswaran, and D. A. Haber, J. Cell. Biol. **192**, 373–382 (2011).
[65] I. J. Fidler, Nat. Rev. Cancer **3**, 453–458 (2003).
[66] D. A. Nedosekin, E. I. Galanzha, E. Dervishi, A. S. Biris, V. P. Zharov. Super-resolution nonlinear photothermal microscopy. Small. June 17. 2013 doi: 10.1002/smll.201300024. [Epub ahead of print].